Noninvasive imaging of epicardial and endocardial potentials with low rank and sparsity constraints

Lin Fang, Jingjia Xu, Hongjie Hu, Yunmei Chen, Pengcheng Shi, Linwei Wang, Huafeng Liu*

Abstract-In this study, we explore the use of low rank and sparse constraints for the noninvasive estimation of epicardial and endocardial extracellular potentials from body-surface electrocardiographic data to locate the focus of premature ventricular contractions (PVCs). The proposed strategy formulates the dynamic spatiotemporal distribution of cardiac potentials by means of low rank and sparse decomposition, where the low rank term represents the smooth background and the anomalous potentials are extracted in the sparse matrix. Compared to the most previous potential-based approaches, the proposed low rank and sparse constraints are batch spatiotemporal constraints that capture the underlying relationship of dynamic potentials. The resulting optimization problem is solved using alternating direction method of multipliers. Three sets of simulation experiments with eight different ventricular pacing sites demonstrate that the proposed model outperforms the existing Tikhonov regularization (zero-order, second-order) and L1-norm based method at accurately reconstructing the potentials and locating the ventricular pacing sites. Experiments on a total of 39 cases of real PVC data also validate the ability of the proposed method to correctly locate ectopic pacing sites.

Index Terms—Inverse problem of electrocardiography, low rank, sparsity.

I. INTRODUCTION

Noninvasive electrophysiological imaging (ECGI), for characterizing and localizing cardiac electrical events from body surface electrocardiograms (ECGs), constitutes a promising strategy for evaluating normal and abnormal cardiac electrophysiology, offering the potential for great impact on cardiac diseases such as ventricular fibrillation [1], premature ventricular contraction (PVC) [2], or ventricular tachycardia (VT) [3]. In particular, the ECGI technique is extensively applied in the precise localization of the PVC origin, for the purpose of facilitating the planning of, and thereby simplifying and shortening, the electrophysiological procedure.

Manuscript received November 21, 2017; revised January 10, 2019; accepted January 12, 2019. Date of publication xxx xx, xxxx; date of current version January 22, 2019. This work is supported in part by National Key Technology Research and Development Program of China (No: 2017YFE0104000, 2016YFC1300302), by the National Natural Science Foundation of China (No: 61525106, 61427807, U180920013, 61701436, 81873908), by Shenzhen Innovation Funding (No: JCYJ20170818164343304, JCYJ20170816172431715), by National Science Foundation CAREER Award under Grant ACI-1350374.

- L. Fang and H. Liu are with the State Key Laboratory of Modern Optical Instrumentation, Department of Optical Engineering, Zhejiang University, Hangzhou 310027, China.
- H. Hu is with the Department of Radiology, Sir Run Run Shaw Hospital, School of Medicine, Zheijang University, Hangzhou 310016, China.
- Y. Chen is with the Department of Mathematics, University of Florida, Gainesville, FL 32611 USA.
- J. Xu, P. Shi and L. Wang are with the Computational Biomedicine Laboratory, Golisano College of Computing and Information Sciences, Rochester Institute of Technology, Rochester, NY 14623 USA.
 - *Corresponding author: H. Liu (email: liuhf@zju.edu.cn).

In order to determine the focus of the origin of cardiac electrical activity, various ECGI approaches have previously been proposed within different scopes. A traditional approach is the use of current dipoles. The concept of using a single dipole to represent intracardiac electrical activity originated in [4]. Subsequently, improved equivalent generators, such as moving dipoles [5], [6] or multiple dipoles [7], [8], have been developed. While these approaches specialize in localizing electrical events in the heart, the solutions contain limited information about the spatiotemporal pattern of the cardiac electrical activity.

Alternatively, potential-based electrophysiological imaging provides intracardiac potential estimates from the body surface potentials. Various regularization techniques have been performed at solving the illposed inverse problem of cardiac potential imaging. In [9], Tikhonov regularization [10], [11] and the generalized minimal residual (GMRes) iterative technique [12], [13] were used to reconstruct epicardial potential sequences, from which the PVC origin was located by means of the local negative potential minimum of early activation. However, L2-norm based methods inherently provide smoothed solutions, and therefore offer compromised accuracy in capturing the PVC origin site [2]. In order to overcome the drawback of L2-norm methods, more recently, Ghosh and Rudy [2] developed a sparse-based L1-norm scheme for epicardial potential reconstruction and locating the epicardial pacing sites, where the L1-norm method outperformed the quadratic methods in terms of accuracy. Further works were later presented to improve the stability and convergence of this method [14], [15]. However, these methods limit the positioning of the pacing site to the epicardium. Therefore, in [16], transmural regularization combined with temporal spline interpolation was used to estimate the potential on the inner (endocardial) as well as outer (epicardial) ventricle surfaces in order to locate the pacing sites. From the estimated potential sequence, the activation time at each node was estimated by the time with the most negative derivative, and the pacing site was located at the earliest activation point. Recently, much attention has been given to approaches that incorporate temporal constraints, such as Kalman filter [17] and doubly truncated singular value decomposition (TSVD) regularization [18].

Typically, another type of ECGI work is activation imaging, which involves estimating the activation times that generate a QRS complex that best fits the recorded QRS on the body surface [19]. Numerous endeavors have been made to reconstruct the activation time on the heart surface [20]–[24] or throughout 3D ventricles [25]–[31]. The solution of activation time, which

indicates the arrival time of the action potential depolarization of the cardiomyocytes, has an explicit interpretation of the "wavefront" behavior of cardiac activation [32] with a clear physiological meaning and can be directly used in clinic. While solution of potentials often needs a further deduction to obtain useful parameters. Thus, activation imaging is very well applied to provide valuable clinical information in simple or complex activation patterns [25], [29]. One of the applications is to find the focus of an arrhythmia (eg., PVC [25]), namely, the site with the earliest activation. It is worthy to mention that there are some new methods for activation imaging based on the temporal (time/frequency) characteristics [25], [28], [31] of equivalent current density, typically, the exploitation of sparsity in the time domain [25], [28] and gradient sparsity in frequency domain [29]. On the other hand, potential based approach may has more versatility. It can not only recover the information from the active band (QRS complex), but also provide the information from the repolarization wave (ST segment or T wave) [33]. Technically, it can estimate the potential distribution on the myocardial surface or within the myocardium tissue at any time during the cardiac cycle. In addition, more parameters may be derived from the potential based reconstruction [29].

In this paper, a new spatiotemporal low rank and sparse decomposition (LSD) framework has been proposed to reconstruct dynamic extracellular endo- and epicardial potential (EEP) and localize the PVC origin. Based on the electrophysiological property of myocardial tissue, when depolarization occurs, a rapid change in ion permeability of the myocardial cell membrane cause ions to rapidly cross the cell membrane, which causes a shift of the extracellular potential, resulting in potential spikes, as pointed in Fig. 1(a) (left). In the rest of the cardiac cycle, myocardial tissue remains almost static. These spikes (potential foreground) account for a relatively small proportion of the space-time distribution of potentials, which are sparse. The remainder (potential background) consists of some of the lower amplitude, relatively flat potentials, which can be low rank for its physical spatiotemporal correlation. This property exists because of the EEP dynamic is spatially smooth and temporally self-similar. That is, the background potentials tend to lie within a low-rank subspace, as illustrated in the empirical results provided in Fig. 1(b). Moreover, the sparse outliers, namely potential spikes, are annotated by the high potential peaks (red) and low potential valleys (blue) in the spatial-temporal map in Fig.1(c).

The novelty of the potential-based LSD method proposed in this study is twofold:

- 1) Low rank is a batch constraint that makes use of the underlying spatiotemporal correlation of electrophysiological dynamics to provide accurate reconstruction.
- 2) Compared to previous smooth/sparse assumption (spatial or/and temporal), we do not mandate that the potential is smooth or sparse, but the appropriate combination of the two components. Therefore, the proposed method may be applicable to extensive cardiac electrophysiological dynamics. In addition, it is not necessary to make assumptions on the explicit form of the potential to be evaluated, compared to some state model based methods such as Kalman filter.

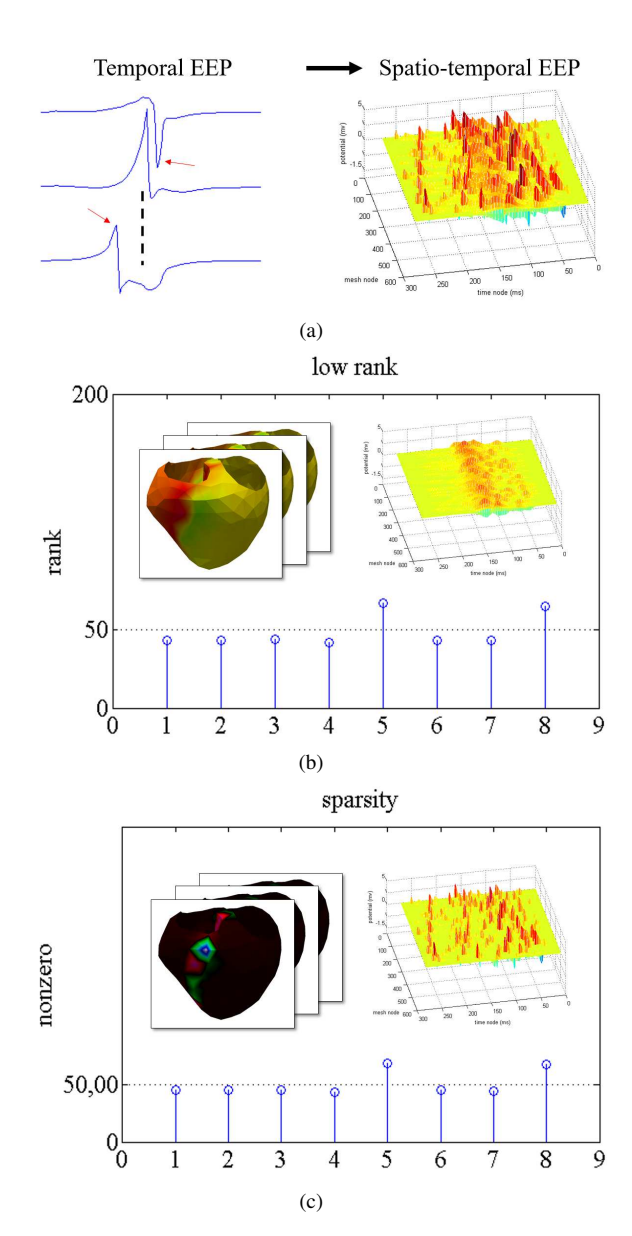


Fig. 1. Rank and sparsity statistics for decomposition of EEP spatiotemporal-distribution matrix ${\bf U}$ of eight simulated ventricular pacing cases. The geometric model of the heart consists of 502 mesh nodes. Each case takes 250 frames in time; that is, ${\bf U} \in R^{502 \times 250}$ for each case. (a) Temporal distribution of EEP for all heart nodes (left) and spatial-temporal EEP dynamic. (b) Low rank part of EEP matrix ${\bf U}$ (x-axis: case number, y-axis: rank). The rank of the background part for each case is approximately 50, which is significantly smaller than the dimension 250 or 502 of the matrix. (c) Sparse part of ${\bf U}$ (x-axis: case number, y-axis: non-zero elements). The number of non-zero elements in the foreground part is approximately 5000, substantially less than the total number of matrix elements 125500 (502*250). Therefore, the spatiotemporal distribution matrix of the EEP can be decomposed into a low-rank background and sparse foreground.

Therefore, the approach can be applied to ventricles with structural lesions.

In order to demonstrate the effectiveness of the proposed method, we implemented a series of experiments on simulated data and real patient data. Firstly, to estimate the accuracy of the proposed LSD method quantitatively in EEP reconstruction, we performed simulation experiments considering eight different pacing sites. For each case, three EEPbased quantities were quantitatively analyzed: EEP spatial distribution, cardiac electrograms, and activation times. The accuracy of the solutions of the zero-order and second-order Tikhonov methods (uniformly abbreviated as Tikhonov-0 and Tikhonov-2 in the following text) and an L1-norm based method were used for comparison with the proposed method. Furthermore, real data experiments were carried out on two patient sets. The first set of experiments were performed on ECG data corresponding to 33 different pacing sites paced on the healthy ventricles of a subject. The second set of experiments were carried out with clinical data of six PVC patients. By comparing the location of the ventricular ectopic pacing site captured by the LSD method to that detected by Ensite3000 system (gold standard), the proposed method was confirmed to locate the ectopic pacing site position correctly.

II. METHOD

In this section, we present the LSD framework to solve the ill-posed inverse problem of dynamic cardiac electrophysiological imaging. Firstly, we introduce the forward model of the ECG imaging problem. The boundary element model (BEM) is adopted to model the relationship between the EEP and BSP. Thereafter, the LSD framework is developed to reconstruct the EEP from the body surface ECG. Finally, a mathematical method for obtaining the optimal solution is designed for the proposed LSD model, and the corresponding iterative algorithm is introduced in detail.

A. Forward Model of Electrocardiography

In this part, we model the forward relationship between the EEP and BSP. In particular, the heart surface model, unlike the popular standard "capped" full-heart epicardial model, is a union of the "uncapped" ventricular epicardium and endocardium. For ease of description, Thereafter, the "heart surface" refers to both the epicardium and endocardium. According to existing work [16], the relationship between the potentials of our equivalent electrical source and the body surface can still be formulated by the standard Laplace equation, based on the quasi-static and isotropic assumptions. Thus, the cardiac electric field between the heart and body surfaces can be expressed by:

$$\sigma_v \nabla^2 \varphi_v \left(\mathbf{r} \right) = 0 \tag{1}$$

where σ_v is the torso conductivity scalar, and $\varphi_v\left(\mathbf{r}\right)$ represents the potentials boundaried between the heart and body surfaces, generated by cardiac electrophysiological activity.

We can solve the Laplace equation (1) by means of the BEM [34]. Then, the forward relationship between the EEP and BSP can be modeled as

$$\phi = \mathbf{H}\mathbf{u} \tag{2}$$

$$\phi \in R^{N \times 1}$$
 $\mathbf{u} \in R^{M \times 1}$ $\mathbf{H} \in R^{N \times M}$

where ϕ is an N-dimensional column vector representing the potentials measured by N-lead electrodes on the body surface; \mathbf{u} is a column vector of the M-dimensional cardiac EEP; and \mathbf{H} is a time-invariant transfer matrix that is specific to the heart-torso geometric model of each subject. The heart-torso model can be obtained from the patient's individual preprocedural thoracic CT scan, which will be detailed in section III.

B. Multi-frame EEP-BSP Model

As illustrated in Fig. 1(a), in order to consider a time sequence of body surface potentials: $\Phi = [\phi_1, \phi_2, \cdots, \phi_f, \cdots \phi_F], \ \phi \in R^{N \times 1} \ \Phi \in R^{N \times F},$ where ϕ_f represents the f-th frame of the body surface potentials, and the corresponding time sequence of the heart surface potential matrix: $\mathbf{U} = [\mathbf{u}_1, \mathbf{u}_2, \cdots, \mathbf{u}_f, \cdots, \mathbf{u}_F],$ $\mathbf{u} \in R^{M \times 1} \ \mathbf{U} \in R^{M \times F},$ where \mathbf{u}_f is the f-th frame of the heart epicardial and endocardial extracellular potentials, the EEP-BSP model (2) of a single-frame ECG can be extended to the multiple-frame form as

$$\mathbf{\Phi} = \mathbf{H}\mathbf{U}.\tag{3}$$

C. Low Rank and Sparsity Formulation

As illustrated in Fig. 1, we analyze the dynamic ECG inverse problem from the image perspective. Fig. 1(a) (left) depicts the dynamic EEP signals over a fragment of ventricular pacing rhythm. The data of single-frame EEPs can be represented by a column vector. Then, the vectored multi-frame EEPs over the cardiac cycle can compose a spatiotemporal distribution image, as illustrated in Fig. 1(a) (right). Although the electrophysiology of the heart exhibits complex spatiotemporal changes, the spatiotemporal distribution of the EEP is locally smooth in space and self-similar in time (certain mesh nodes exhibit similar patterns of cardiac electrogram, as illustrated in Fig. 1(a) (left)). Therefore, the underlying background of the dynamic EEP may be low-rank, as indicated in Fig. 1(b), while the remaining potential outliers are sparse, as depicted in Fig. 1(c). Thus, the spatiotemporal EEP matrix U can be expressed as

$$\mathbf{U} = \mathbf{L} + \mathbf{S} \tag{4}$$

where the low-rank matrix \mathbf{L} can be interpreted as the low-level background of the spatiotemporal EEP, and the sparse matrix \mathbf{S} can be expressed as "unaligned" details, such as the wavefront of the electrical activation propagating over the heart surface.

Owing to the ill-posedness of the electrophysiological inverse problem, small noise will result in a large error in the solution. By enforcing a low-rank background and sparse features for the spatiotemporal EEP distribution, the disturbance of noise in the reconstruction can be eliminated to a certain extent. Eventually, the LSD framework can be expressed as a constrained minimization problem:

$$\min \quad rank(\mathbf{L}) + \lambda \|\mathbf{S}\|_{0} \tag{5}$$

$$s.t.$$
 $\Phi = HU$ $U = L + S$

where $rank(\mathbf{L})$ indicates the rank of \mathbf{L} ; $\|\mathbf{S}\|_0$ is the L0 norm of \mathbf{S} , namely the number of non-zero elements in \mathbf{S} ; and λ is a parameter that balances between the two terms.

However, the minimization problem of the objective (5) is NP hard, as both the matrix rank and L0 norm are non-convex and discontinuous. Fortunately, the minimization of the nuclear norm is a convex relaxation of the rank minimization problem [35], and the L1 norm is a convex approximation of the L0 problem [36]. Therefore, we can solve the optimization target approximately using the following objective function:

$$\min \quad \|\mathbf{L}\|_* + \lambda \|\mathbf{S}\|_1$$

$$s.t. \quad \mathbf{\Phi} = \mathbf{H}\mathbf{U} \quad \mathbf{U} = \mathbf{L} + \mathbf{S}$$
(6)

where $\|\mathbf{L}\|_*$ is the nuclear norm of matrix \mathbf{L} ; that is, the sum of the singular values of \mathbf{L} ; and $\|\mathbf{S}\|_1 = \sum_{ij} |\mathbf{S}_{ij}|$ is the L1 norm of matrix \mathbf{S} by treating matrix $\mathbf{S}(M \times F)$ as a long vector in $R^{M \cdot F}$.

Moreover, because of the disturbance of Gaussian noise in the system, the forward constraint $\Phi = HU$ cannot be strictly established. The error can only be minimized by optimization, as follows:

min
$$\|\mathbf{L}\|_* + \lambda \|\mathbf{S}\|_1 + \frac{\mu}{2} \|\mathbf{H}\mathbf{U} - \mathbf{\Phi}\|_F^2$$
 (7)
 $s.t. \quad \mathbf{U} = \mathbf{L} + \mathbf{S}$

where the Frobenius norm $\|A\|_F$ is defined for any matrix $A(m \times n)$ as $\|A\|_F = \sqrt{\sum\limits_{i=1}^m \sum\limits_{j=1}^n |a_{ij}|}$, and μ is another parameter controlling the contribution of the data fitting term to the objective function.

D. Optimal Estimation Strategy

In this paper, the alternating direction method of multipliers (ADMM [37]) is used to solve the LSD optimization problem in formula (7). Thus, the augmented Lagrangian function for the constrained minimization problem in (7) can be formulated as an unconstrained equation:

$$\mathcal{L}(\mathbf{L}, \mathbf{S}, \mathbf{U}) = \|\mathbf{L}\|_* + \lambda \|\mathbf{S}\|_1 - \langle \mathbf{Z}, \mathbf{U} - (\mathbf{L} + \mathbf{S}) \rangle + \frac{\beta}{2} \|\mathbf{U} - (\mathbf{L} + \mathbf{S})\|_F^2 + \frac{\mu}{2} \|\mathbf{H}\mathbf{U} - \mathbf{\Phi}\|_F^2$$
(8)

where **Z** is a Lagrangian multiplier, and λ , β , and μ are weighting factors. It is difficult to solve all of the unknown matrices **L**, **S**, and **U** directly. In this paper, we decompose the augmented Lagrangian function (8) into two types of sub-problems, and then solve each sub-problem by alternate updating and successive iterations.

1) L, S Sub-problem: According to the theory mentioned in [38], the minimization of the rank problem formulated as the following form:

$$\min \ \varepsilon \|X\|_* + \frac{1}{2} \|X - Y\|_F^2 \tag{9}$$

can be solved directly by means of singular value thresholding (SVT). We obtain the solution as

$$X = SVT(Y) = U_Y S_{\varepsilon}(\Sigma) V_Y^T$$
 (10)

where X and Y are matrices of the same dimension, and $U_Y \Sigma V_Y^T = Y$ is the singular value decomposition of Y. Moreover, $\Sigma = diag(\gamma_1, \cdots \gamma_i, \cdots \gamma_n)$ is a diagonal matrix with all singular values of Y as diagonal elements, and $S_{\varepsilon}(\Sigma)$ is the soft shrinkage of Σ , which is defined for every element of Σ as $S_{\varepsilon}(\gamma) = \operatorname{sgn}(\gamma) \cdot \max(|\gamma| - \varepsilon, 0)$.

We separate all of the terms related to $\bf L$ from the augmented Lagrangian function (8) and provide the necessary constants to construct a frame-like formula (9). Then, the L sub-problem can be structured as

min
$$\|\mathbf{L}\|_* + \frac{\beta}{2} \|\mathbf{L} - (\mathbf{U} - \mathbf{S} + \mathbf{Z}/\beta)\|_F^2$$
. (11)

According to the above theory, we can adopt SVT to solve the minimum rank problem directly. The solution to the L sub-problem can be formulated by the following equation and subjection:

$$\mathbf{L} = U_{Y_L} S_{1/\beta} (\Sigma_{Y_L}) V_{Y_L}^T$$

$$s.t. \quad Y_L = \mathbf{U} - \mathbf{S} + \mathbf{Z}/\beta.$$
(12)

Similarly, the S sub-problem can be structured as

min
$$\lambda \|\mathbf{S}\|_1 + \frac{\beta}{2} \|\mathbf{S} - (\mathbf{U} - \mathbf{L} + \mathbf{Z}/\beta)\|_F^2$$
. (13)

Soft shrinkage [36] has been exploited to calculate the optimal solution of the sparse (L1 norm) problem. The solution can be obtained by one step as

$$\mathbf{S} = S_{\lambda/\beta} (Y_S)$$

$$Y_S = \mathbf{U} - \mathbf{L} + \mathbf{Z}/\beta$$
(14)

2) U Sub-problem: The U sub-problem is composed of two F-norm fidelity terms and an inner product term containing a Lagrange multiplier. It can be reformulated as

min
$$\frac{\mu}{2} \|\mathbf{H}\mathbf{U} - \mathbf{\Phi}\|_F^2 + \frac{\beta}{2} \|\mathbf{U} - (\mathbf{L} + \mathbf{S} + \mathbf{Z}/\beta)\|_F^2$$
. (15)

This is a convex minimization problem, and the solution can be expressed directly as

$$\mathbf{U} = (\mu \mathbf{H}^T \mathbf{H} + \beta)^{-1} [\mu \mathbf{H}^T \mathbf{\Phi} + \beta (\mathbf{L} + \mathbf{S} + \mathbf{Z}/\beta)]. \quad (16)$$

By solving the sub-problems alternately, we can obtain the optimal solution to the LSD model. The complete algorithm is summarized in Algorithm 1.

E. Algorithm Summary

Initialization: In order to overcome the mathematical ill-posedness of the inverse problem, Tikhonov-0 regularization is applied to initialize the EEPs prior to the first iteration as: $\mathbf{U}^0 = (\mathbf{H}^T \mathbf{H} + \lambda_0 \mathbf{I}^T \mathbf{I})^{-1} \mathbf{H}^T \mathbf{\Phi}$, where \mathbf{I} is an identity matrix. The weighting coefficient λ_0 can be estimated by means of the L-curve method [39].

Parameters: λ, β , and μ are scalars to balance the minimization target. Among these, λ is weighting parameter of the sparse matrix \mathbf{S} . According to the theorem in [36], $1/\sqrt{\max(m,n)}$ is an appropriate selection for λ , where the dimension of \mathbf{S} is $m \times n$. Moreover, β is a Lagrangian penalty parameter, which lies within [0.01, 0.1] in this study, and μ is the coefficient of fidelity term, determined by the noise

Algorithm 1 LSD Algorithm

Require: BSP matrix Φ , transfer matrix H, weighting coefficients λ , β , μ

1: Initialize: $\mathbf{U}^0 = (\mathbf{H}^T \mathbf{H} + \lambda_0 \mathbf{I}^T \mathbf{I})^{-1} \mathbf{H}^T \mathbf{\Phi}, \ \mathbf{L}^0 = \mathbf{S}^0 =$ $0, \mathbf{Z}^0 = 0$

- 2: repeat
- Update \mathbf{L}^{k+1} by formula (12) 3:
- Update S^{k+1} by formula (14) 4:
- Update U^{k+1} by formula (16) 5:
- Update \mathbf{Z}^{k+1} :

$$\mathbf{Z}^{k+1} = \mathbf{Z}^k + \delta_k \left(\mathbf{U}^{k+1} - \mathbf{L}^{k+1} - \mathbf{S}^{k+1} \right)$$

 $\delta_{k+1} = \begin{cases} \rho \delta_k & \text{if } \delta_k \big\| \mathbf{S}^{k+1} - \mathbf{S}^k \big\|_F / \big\| \mathbf{U}^{k+1} \big\|_F < \varepsilon \\ \delta_k & \text{else} \end{cases}$ 8: **until L**, **S**, **U** are all converged

Ensure: L, S, U

intensity. For the experiments presented in this paper, μ is fixed at 0.5. Furthermore, τ , ρ , and ε affect the convergence speed and are fixed at 0.1, 1.2, and 0.1, respectively.

III. EXPERIMENTS

In this section, the proposed method is evaluated by three types of datasets: 1) simulated ventricular single pacing at eight different pacing sites; 2) real ventricular pacing at 33 sites from the endocardial surface of the healthy ventricles of a subject; 3) and six cases of clinical PVCs. We compared the accuracy of the proposed LSD to that of the L2-normbased Tikhonov-0, Tikhonov-2 regularization, and L1-norm method, which is formulated as: min $\|\mathbf{H}\mathbf{u} - \phi\|_2 + \lambda^2 \|D\mathbf{u}\|_1$ [2], where D indicates the normal derivative operator.

A. Simulation Experiments on Ventricular Pacings

In this section, we discuss the simulation experiments performed considering eight different pacing sites. The endoand epicardial extracellular potential ground truths of the ventricular pacings were obtained from the Internal database - Experimental Data and Geometric Analysis Repository (EDGAR, http://edgar.sci.utah.edu/) [40], where the ventricular beats were simulated on a voxel-based grid using cellular automaton [41], and the extracellular potentials were extracted from a tetrahedral mesh at 163 electrode positions [42]. In this work, the body surface potentials were forward calculated by $\Phi = HU + N$, where N is a matrix of 25 dB white Gaussian noise.

From the reconstructed potential, we examined the following three reconstructed quantities: 1) the spatial distribution map of EEP at a given time node during the pacing rhythm; 2) the electrogram, which illustrates the change of potential at a given mesh node over time; and 3) the map of activation time, which is defined when the negative derivative (-du/dt)of the electrogram reaches a maximum. In order to analyze the reconstruction accuracy quantitatively, the relative errors (RE) and correlation coefficient (CC) between the reconstructed quantities and ground truths were utilized:

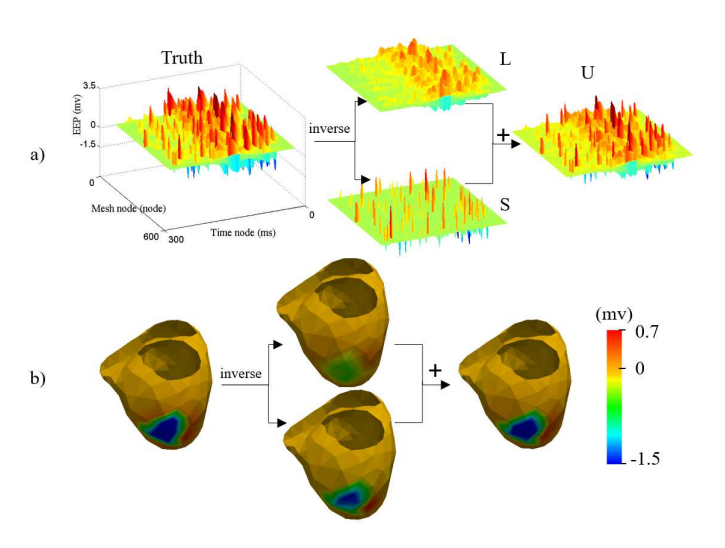


Fig. 2. Reconstruction of EEP by LSD method with pacing site located at lateral left ventricle (LV), where (a) represents a low-rank and sparse reconstruction of a single pacing. Among these, (b) is the spatial distribution of the EEP at approximately 20 ms following the onset of pacing rhythm.

$$RE = \sqrt{\frac{\sum_{i=1}^{M} (x_{r_i} - x_{t_i})^2}{\sum_{i=1}^{M} (x_{t_i})^2}}$$
 (17)

$$CC = \frac{Cov(x_r, x_t)}{\sqrt{D(x_r)}\sqrt{D(x_t)}}$$
(18)

where x_r denotes a column vector of the reconstructed quantity and x_t is the corresponding ground truth. Moreover, M is the number of mesh nodes of the heart surface, $Cov(x_r, x_t)$ is the covariance between the reconstructed quantity and the truth, and $D(\cdot)$ represents the variance.

1) Spatial EEP mapping: Fig. 2(a) provides an example of the dynamic EEP reconstruction over a fragment of cardiac cycle of the lateral LV pacing. The first image, on the left in Fig. 2(a), illustrates the ground truth of the color-scaled spatiotemporal EEP map throughout the pacing rhythm. The two middle maps, from top to bottom, are the low-rank background and sparse foreground of the reconstructed EEP. The rightmost image is the final solution of the EEP reconstruction. The spatial distribution of the EEP at an instant of the initial time (20 ms) was extracted and is illustrated in Fig. 2(b). From the middle two maps, it can be seen that the low-rank component of the EEP reconstruction mainly includes the smooth part of the potential, while the sparse component contains the outlier negative potential valley (blue) and the positive potential wall

Fig. 3 shows the spatial distribution of EEP at four instances (23, 52, 152, and 199 ms) in the process of electrical excitation during the lateral LV pacing, roughly demonstrating the process of electrical activation spreading from the pacing site at the lateral LV to the remote right ventricle (RV). The solutions of Tikhonov-0, Tikhonov-2, and L1-norm methods mentioned in the beginning of this section were used for comparison with the LSD method. The leftmost column in Fig.

TABLE I

MEAN AND STANDARD DEVIATION OF CC AND RE BETWEEN
RECONSTRUCTED AND TRUE ELECTROGRAMS OF EIGHT DIFFERENT
PACING SITES, WHERE THE '±' INTERVAL REPRESENTS THE STANDARD
DEVIATION.

Doning site	Tikhonov-2		L1-norm		LSD	
Pacing site	CC	RE	CC	RE	CC	RE
LV						
anterior	0.64±0.16	0.76 ± 0.33	0.68±0.16	0.67 ± 0.23	0.74±0.18	$0.61 {\pm} 0.25$
apex	0.61±0.20	0.80 ± 0.28	0.62±0.18	0.79 ± 0.19	0.71±0.20	$0.67 {\pm} 0.22$
lateral-endo	0.70±0.18	0.74 ± 0.37	0.70±0.20	$0.66 {\pm} 0.20$	0.73±0.21	$0.61 {\pm} 0.23$
lateral-epi	0.63±0.16	0.79 ± 0.26	0.68±0.17	0.69 ± 0.19	0.68±0.21	$0.66 {\pm} 0.60$
lateral	0.67±0.19	0.74 ± 0.25	0.69±0.18	0.66 ± 0.17	0.77±0.17	$0.58 {\pm} 0.21$
septum	0.62±0.17	0.89 ± 0.47	0.63±0.19	$0.86 {\pm} 0.24$	0.67±0.17	0.70 ± 0.17
RV						
anterior	0.65±0.17	0.76 ± 0.31	0.67±0.18	0.69 ± 0.19	0.73±0.19	$0.62 {\pm} 0.22$
posterior	0.63±0.20	0.76 ± 0.31	0.64±0.19	0.72 ± 0.22	0.73±0.20	$0.58 {\pm} 0.22$

3 illustrates the ground truth, followed by the solutions of the Tikhonov-0, Tikhonov-2, L1 norm, and the proposed methods. According to the comparison, Tikhonov-0 could only roughly denote the position of the negative potential valley and positive potential peak, but the potential pattern is seriously distorted. The overall accuracy of the Tikhonov-2 was improved, but the reconstruction was over-smooth, and the steep gradient between the negative potential valley and positive potential nearby could not be maintained effectively. Compared to the previous two methods based on the L2-norm, the method based on the L1 norm could better maintain steep potential mutation, but in terms of the potential pattern fidelity and quantized reconstruction accuracy, the proposed LSD method was even more superior. The spatial CC and RE at each time node during the pacing rhythm were illustrated in Fig. 4. Spatial CC and RE are the accuracy measures of reconstructed EEP spatial distribution at a certain time.

2) EEP electrogram reconstruction: In Fig. 5, we selected five representative locations to demonstrate the reconstruction of electrograms of the anterior LV pacing. The numbers of these five selected nodes and locations on the heart surface are provided in the leftmost 3D heart model in Fig. 5. Among them, node 162 is located near the pacing site at the anterior LV, and node 256 is located at the inferior LV endocardium. The remaining three nodes are located at RV, remote from the pacing site. The color of the heart model in Fig. 5 indicates the activation time, where the red represents the earliest activation and the blue represents the latest activation. The first column of electrograms in Fig. 5 displays the real electrograms of the given mesh nodes, followed by the electrograms reconstructed by means of the Tikhonov-0, Tikhonov-2, L1-norm, and LSD methods. As can be observed from Fig. 5, Tikhonov-0 can only roughly describe the electrogram trend, with a strong jitter. The Tikhonov-2 and L1-norm methods significantly improve the stability of reconstruction, but the LSD method can better preserve the electrogram shape.

In Table I, the accuracy of the electrograms of the ventricular pacings at eight different sites is quantitatively summarized according to the mean and standard deviation of the temporal CC and RE. Here, temporal CC represents the morphological similarity between the reconstructed and real electrograms, while RE represents the overall error between the recon-

 $\begin{tabular}{l} TABLE~II\\ Localization~errors~of~the~8~simulated~ventricular~pacings. \end{tabular}$

Pacing site	Tikhonov-2	L1-norm	LSD		
LV	localization error (mm)				
anterior	31.65	28.34	14.35		
apex	16.56	8.92	2.82		
lateral-endo	10.68	7.81	4.88		
lateral-epi	5.46	4.84	1.70		
lateral	11.37	11.36	9.22		
septum	35.21	29.45	18.14		
RV					
anterior	21.19	14.05	9.36		
posterior	20.29	24.82	13.17		

structed and true values over time. The average CC/RE in Table I of each pacing case refers to the mean of the CC/RE of electrograms at all 502 mesh nodes (In this experiment, 8 pacing cases share a ventricular geometric model with spatial resolution of 502 mesh nodes).

3) Activation imaging: Here, we evaluate the accuracy of the reconstructed activation time. In order to reduce the error of deriving the activation time from the potentials, a smoothing step has be carried out on the estimated activation times before searching for earliest activation [16]. Fig. 6 illustrates the true and reconstructive behavior of the activation time for a single pace at ventricular septum. The leftmost column in Fig. 6 indicates the real activation map, followed by the reconstruction activation maps by means of Tikhonov-2, L1-norm, and LSD methods, where the color red indicates the earliest activation and the blue indicates the latest activation.

As illustrated in Fig. 6, the Tikhonov-2 method and L1-norm method provide lower accuracy of activation times compared to the proposed LSD method. This is in line with expectation. The LSD method is based on the constraints of the spatiotemporal characteristics of EEP dynamic, and exhibits superior performance in reconstruction of the temporal EEP. As indicated in Fig. 5, due to the lack of temporal constraint, the electrogram revivification degrees of Tikhonov-2 and L1-norm method are inferior to that of LSD method, which negatively affects the calculation of the activation time. Table II lists the localization errors of the pacing sites by finding the earliest activation nodes. The proposed LSD method provides relatively accurate localization in different pacing cases.

B. Real Ventricular Pacings

1) Interventional pacings: In this experiment, 33 cases of real ventricular pacings were produced endocardially using the tip of an ablation catheter. The data in this experiment come from other published work [16], which are shared in the online database EDGAR. A total of 33 ventricular pacing sites were generated at different locations in the left/right ventricle of a subject, and used to evaluate our method quantitatively. The induced body surface potentials were measured by 120 electrodes with a sampling frequency of 2 kHz. The numbers of beats for each pacing site of the subject are displayed in the second column of Table III. The true coordinates of the pacing sites were located by the CARTO XP electroanatomic

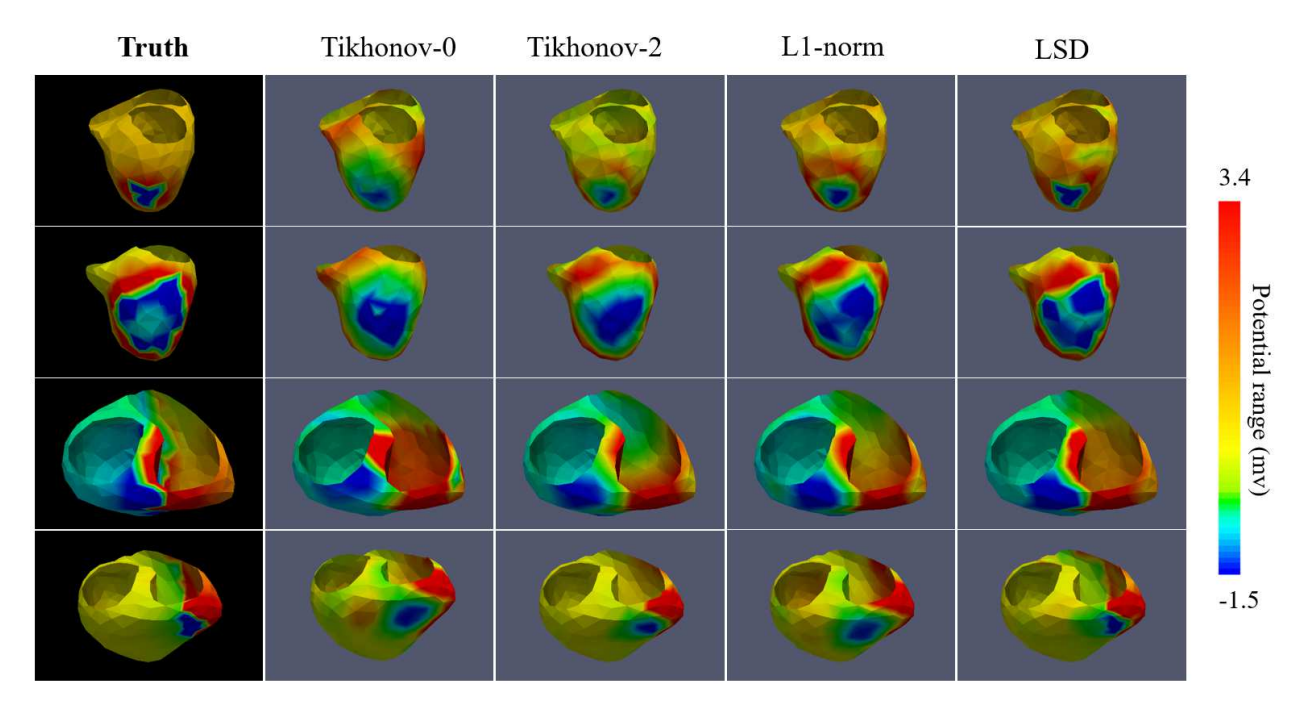


Fig. 3. Reconstruction of spatial EEP at four instants (23ms, 52ms, 152ms, and 199ms) in process of ventricular pacing. Reconstruction accuracy CC and RE are summarized in Fig. 4

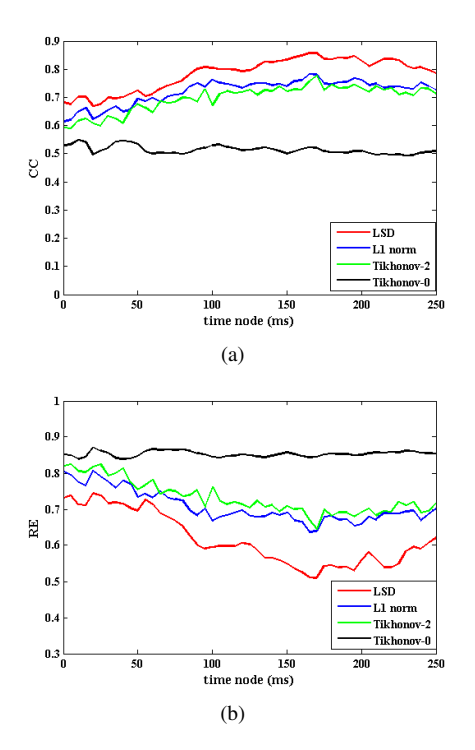


Fig. 4. Comparison of CC and RE of reconstructed spatial EEP for pacing at lateral LV.

mapping system and matched to the 3D heart surface model by the data contributors [16].

Table III lists the localization error of the 33 different ventricular pacing sites by means of the proposed LSD and L1-norm methods. By comparing the mean and standard deviation of the 3D coordinate errors for each pacing site, the proposed LSD method provides more accurate and stable

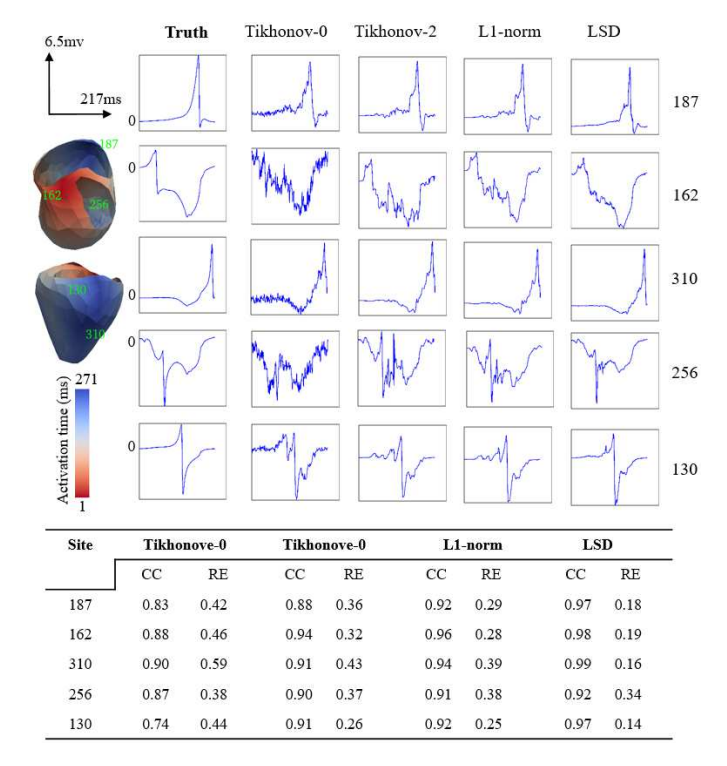


Fig. 5. True and reconstructed electrograms of pacing at anterior LV. The leftmost side shows the real activation map of 271 ms, where the red indicates the earliest activation and the blue indicates the latest activation. EEP electrograms at five selected mesh nodes (Node number: 187, 162, 310, 256, 130) are illustrated by blue curves. The table below lists the CC and RE of the electrograms according to the selected nodes.

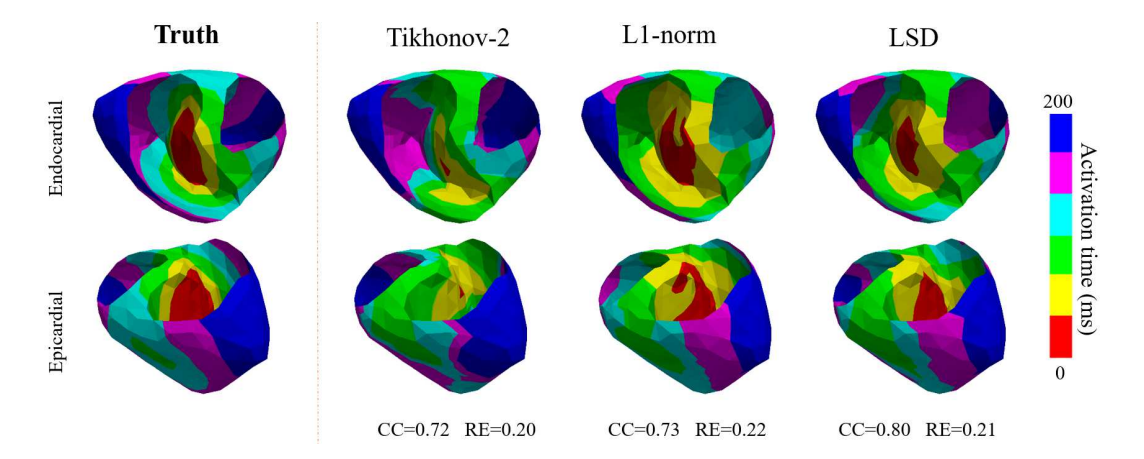


Fig. 6. Reconstruction of activation map for the pacing at the interventricular septum. The top row is endocardial view and the bottom row is epicardial view.

location results than the L1-norm based method. [16] also provided solutions for ventricular pacing sites for this dataset, where spatial transmural gradient regularization and temporal piecewise cubic spline interpolation were used to reconstruct the EEPs. Compared to separate reconstruction at each knot node, as reported in [16], the batch optimization method proposed in this paper provides higher accuracy in terms of localizing pacing sites, potentially owing to the use of the entire ECG sequence instead of ECG data at the knot points for localization.

2) Clinical PVCs: In this part, the localization experiments of PVC focus were performed with 6 sets of clinical data. The individual geometric and positional information of the heart and torso were recorded by CT scan with a spatial resolution of axial 0.6-1 mm. Fig. 7 explicitly illustrates the establishment process of the heart-torso modeling. The heart model was established by meshing the epicardial and endocardial contours extracted from the CT slices (512*512 pixels) of the ventricle along the short axis. The torso model was constructed by matching the coordinates of body-surface electrodes to a standard tank model with 235 triangles of Delaunay triangulation. The positions of the 64 electrodes are recorded by CT scan, and the distribution of the electrodes is illustrated in Fig. 8. 64-lead ECGs contain multiple consecutive cardiac cycles, sampled at 2 kHz.

Most PVCs originate from the RV, especially the right ventricular outflow tract (RVOT), with a small part of them originating from the LV [43]. Therefore, this experiment focused on a case of PVC originating from the LV apical free wall, and five cases of PVC originating from different RVOT locations (anterior, posterior, septum, and free wall). The correctness of the reconstruction was evaluated by comparing the PVC focus revealed by LSD-based electrophysiological imaging to that obtained from the intraoperative Ensite3000 system.

Fig. 9(a) illustrates the intraoperative ECG fragment of the 25th electrode of a 52-year-old male PVC patient with a ectopic pacing site located at the LV apex. The location of the 25th electrode is marked in Fig. 8. This ECG fragment exhibits the following characteristics: 1) premature contractions and sinus heartbeats appear alternately; and 2) the premature QRS

TABLE III

MEAN AND STANDARD DEVIATION OF LOCALIZATION ERRORS FOR INTERVENTIONAL PACINGS.

Pacing site		L1-norm		LSD		
LV	beats	mean (mm)	std (mm)	mean (mm)	std (mm)	
1	43	27	7	24	4	
2	18	28	5	25	4	
3	38	26	6	22	3	
4	41	26	10	19	6	
5	35	24	4	22	3	
6	35	36	10	26	8	
7	27	24	6	20	5	
8	14	37	10	24	9	
9	29	30	14	22	4	
10	32	27	9	21	9	
11	33	23	9	18	5	
12	37	28	10	21	4	
13	30	34	7	27	7	
14	21	26	10	22	7	
15	28	28	8	22	5	
16	35	33	9	26	5	
17	33	21	8	18	6	
18	32	28	13	19	6	
19	35	27	6	23	3	
20	24	27	8	21	3	
21	34	35	11	21	5	
RV	beats	mean (mm)	std (mm)	mean (mm)	std (mm)	
1	17	25	6	20	4	
2	12	27	12	23	8	
3	30	26	8	20	6	
4	35	31	11	23	5	
5	34	30	7	26	2	
6	34	23	5	20	2	
7	31	23	6	20	4	
8	7	25	8	22	4	
9	33	23	6	21	5	
10	13	20	4	18	2	
11	27	28	11	22	7	
12	17	25	10	16	4	
12	1 ,	1 23	10	1	•	

wave is broader than the normal QRS wave; for example, the first premature QRS wave in Fig. 9(a) begins at 15207 ms and ends at 15347 ms, with a time span of 0.14 s, and is broader than 0.12 s of the normal QRS wave. According to the electrocardiogram morphology, this subject was diagnosed with frequent ventricular premature beats. The precise PVC focus is indicated by the activation map provided by the Ensite3000 system in Fig. 9(b), which reveals ventricular

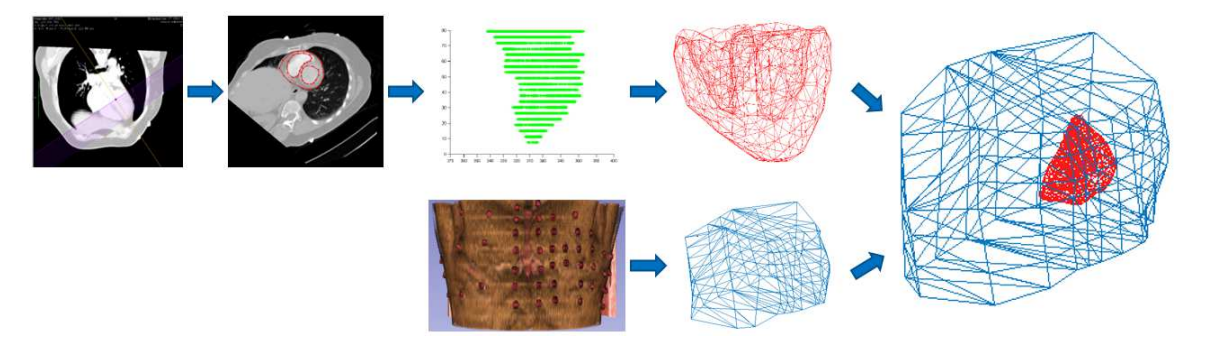


Fig. 7. Establishment process of heart-torso model. The top line illustrates the heart modeling process, and the bottom line depicts the details of building the torso geometric model.

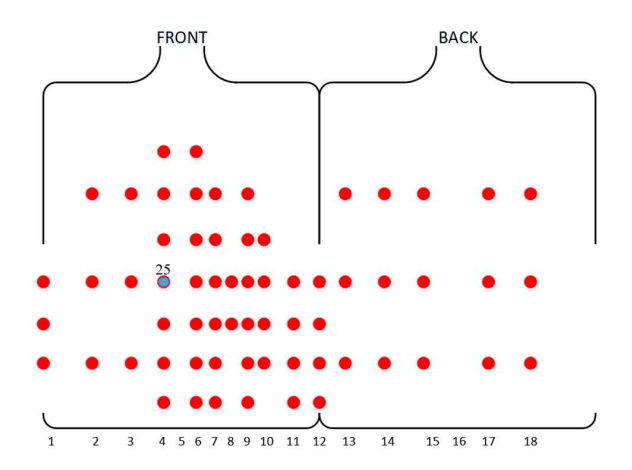


Fig. 8. Positions of 64-lead electrodes on body surface. The left side represents the front view of the body surface, and the right side represents the back view.

ectopic pacing at the left apical free wall.

The ECGs from 15000 ms to 16000 ms were used as the input for the LSD method. Fig. 9(c) illustrates the spatial distribution of the EEP at 15 ms after the onset of the QRS wave, when a negative potential valley (blue) appears at the LV apex with the positive potential wall (red) surrounds it, implying the ectopic pacing site at the left apical free wall. Fig. 9(d) illustrates the reconstructed activation mapping. The activation from the earlier to later stage is expressed by colors from red to blue, where earlist activation site is at the LV apex, consistent with the invasive mapping data.

Fig. 10 presents five clinical PVCs originating from different locations of RVOT. The first image in each row of Fig. 10 represents a 2500 ms fragment of an electrocardiogram measured by the 25th electrode placed at the front center of each patient body. During this period, the ECG fragment enclosed by the red dashed box is a premature cardiac cycle used as input to the ECG inverse problem. The second image of each row in Fig. 10 is the right ventricular outflow tract model and activation map reconstructed by the invasive Ensite3000 system, which serves as the gold standard for assessing the correctness of computing the results using the proposed method, where the red globule represents the ablation target; that is, the ectopic pacing site location. The activation time is represented by a

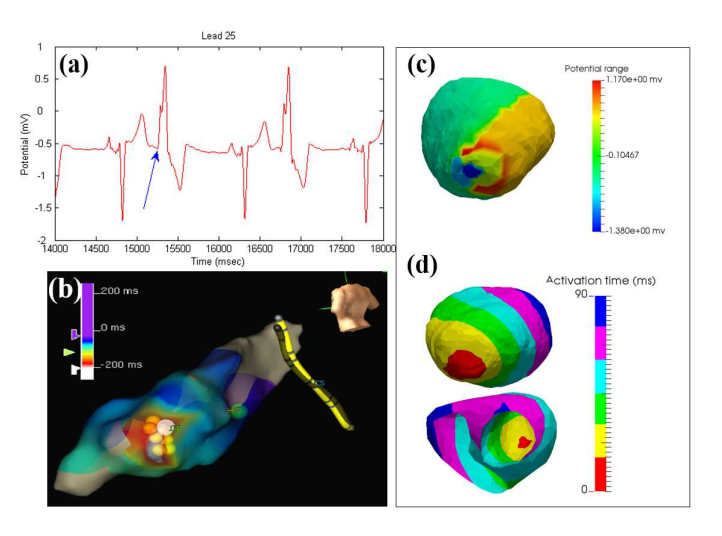


Fig. 9. Diagnosis of frequent PVC at LV apex free wall. (a) ECG fragment measured by the 25th lead. The blue arrow refers to the start of the premature excitation. (b) Intraoperative activation mapping of Ensite3000 system. (c) Reconstruction of spatial EEP at 15 ms after onset of QRS wave. (d) Reconstruction of activation map.

white to purple color bar at the bottom of the second column. The last two images of each row in Fig. 10 is activation maps obtained by performing a maximum negative gradient operation on the cardiac electrocardiogram reconstructed by the LSD method. The activation time begins from the onset of the QRS wave of the input cardiac cycle, where the color ranges from red to blue, indicating activation from earlier to later. And the red color marks the earliest activation, which is the position of the ectopic pacing site.

Case 1 is the diagnosis of a 58-year-old female patient with PVC. The Ensite3000 intraoperative diagnosis revealed that the origin of the premature beat was located below the pulmonary valve in the anterior RVOT. The activation map reconstructed by the LSD-based electrophysiological imaging method also correctly indicates the earliest activation, located at the anterior RVOT, which is consistent with the intraoperative measurement, where the RVOT is an infundibular extension of the right ventricular cavity in the 3D ventricular model. In case 2, the diagnosis of the PVC originating from the anterior RVOT was similar to that in case 1, but for frequent ventricular premature beats. And it can be concluded from

the electrocardiogram that the premature and normal pacing appeared alternately. In this case, the proposed method can still correctly prompt the earliest activation site, which is consistent with the intraoperative diagnosis. In the following three cases, the ectopic pacing sites were located at the front free wall of the RVOT below the pulmonary valve, the RVOT septum near the ventricular septal side, and the posterior RVOT. In the reconstructed activation maps of these different PVC origins, it is observed that the proposed LSD method can correctly locate the earliest activation position, which is consistent with the results constructed by means of an invasive method.

IV. DISCUSSION

This paper has introduced a dynamic EEP reconstruction method based on low rank and sparsity constraints. Compared to previous work on locating the PVC origin, the proposed model provides dynamic constraints and a batch optimization scheme, with no need for a tough assumption regarding the form of the cardiac potential. Thereby, the method improves the reconstruction accuracy by exploiting the underlying relationships of the dynamic EEP. Moreover, the dynamic EEPs are batch calculated, avoiding the cumbersomeness of frameby-frame calculations in previous single-frame-based methods, where the calculation time increases linearly with the sample time. However, solving the low-rank problem requires performing a singular value decomposition of a large matrix (for example, in the experiment in section III-A-1, the dimension of the EEP matrix U is 502×272), which increases the computation time. Furthermore, the multi-constrained minimization goal increases the number of balanced parameters. In this section, we compare the computation times of the Tikhonov-0, Tikhonov-2, L1-norm, and LSD methods. The influence of the LSD parameter setting on the solution stability and the limitations of this work are also discussed.

A. Parameter Setting

In this paper, the ADMM method was applied to solve the LSD model. The three balance parameters λ , β , μ were used to balance the minimum objective function (8). For fixed λ , β , μ , the difference between the value of the objective function and constraint at the n-th iteration and optimal value is O(1/n) [37]. We used CC and RE to quantitatively evaluate the accuracy of the reconstruction. It is worth mentioning that the LSD model uses low rank/sparsity as a condition for optimization, but does not use a fixed rank or sparsity as a criterion for decomposition. Therefore, the accuracy of the decomposition itself cannot be quantitatively evaluated. Here we only discuss the robustness of the accuracy of reconstruction to the balance parameters.

Since λ is fixed to $1/\sqrt{\max(m,n)}$ [36], where m and n represent the number of rows and columns of the solution, respectively. In order to explore the the LSD solution stability under different settings for the balance parameters, we compare the CC and RE between the reconstruction quantity (cardiac electrogram) and true value within a given parameter range for β and μ , where μ is set within [0.001, 1] when β

TABLE IV

COMPARISON OF COMPUTING TIMES FOR EEP RECONSTRUCTION BY

MEANS OF DIFFERENT METHODS.

Site (frames)	Tikhonov-0	Tikhonov-2	L1-norm	LSD
lateral (272)	91.7 s	92.2 s	568 s	293 s
anterior (217)	73 s	73 s	510 s	282 s
septum (200)	68 s	68 s	401 s	135 s

is fixed at 0.01, and β is tested from 0.0001 to 0.1 when μ is fixed at 0.5.

Fig. 11 illustrates the variation trend of the CC and RE averages for spatial EEPs of an example of lateral LV pacing under different μ and β settings. Figures 11(a) and 11(b) indicate that when μ is between 0.001 and 1, the average CC is between 0.8113 and 0.8118, and RE is between 0.4460 and 0.4464. The CC and RE values are relatively stable when $\mu > 0.2$. As can be observed from Figs. 11(c) and 11(d), CC and RE are more sensitive to β when β is less than 0.01, and tend to be stable when $\beta > 0.01$.

B. Computing Time

Table IV summarizes 3 examples of the time spent on EEP reconstruction with different pacing sites (lateral LV, anterior LV, and septum) from the experiment discussed in section III-A by means of the four ECG inverse methods used in this paper. The number of mesh nodes of the heart model is 502, and the number of time nodes of the cardiac cycle for different paced sites is indicated by the number in parentheses in the first column of Table IV. All computations were processed by MATLAB R2014a with a 3.4 GHz processor and 8 GB RAM.

The Tikhonov-0 and Tikhonov-2 methods, based on the L2-norm, are single-frame non-iterative operations, and offer additional advantages in terms of time cost than the latter two iterative algorithms. The L1-norm method is a single-frame iterative algorithm, which requires iterative calculations for each frame of the entire cardiac cycle, thereby taking a relatively long time. The proposed LSD algorithm treats multi-frame vectorized EEPs as an image matrix, and spends most of the time on singular value decomposition and matrix inversion. There is a certain improvement in time spending compared to the L1-norm-based single-frame iterative algorithm, as indicated in Table IV.

C. Limitations

In this paper, in order to reduce the complexity of the heart-torso model, the unnecessary restriction of tissue anisotropy or inhomogeneity were simplified to make the source/data relationship subject to the electric field law inherent in Laplace equation. At the same time, the heart model is simplified to a double-layer "un-capped" surface consisting of endocardium and epicardium of the ventricles, without the rest of the heart tissues such as the atrium. Therefore, the proposed model can not simultaneously perform electrophysiological imaging of the atrial and ventricular surfaces close to atrium due to modeling errors. If electrophysiological remodeling of the atria is required, an independent atrium geometric model [44] is needed.

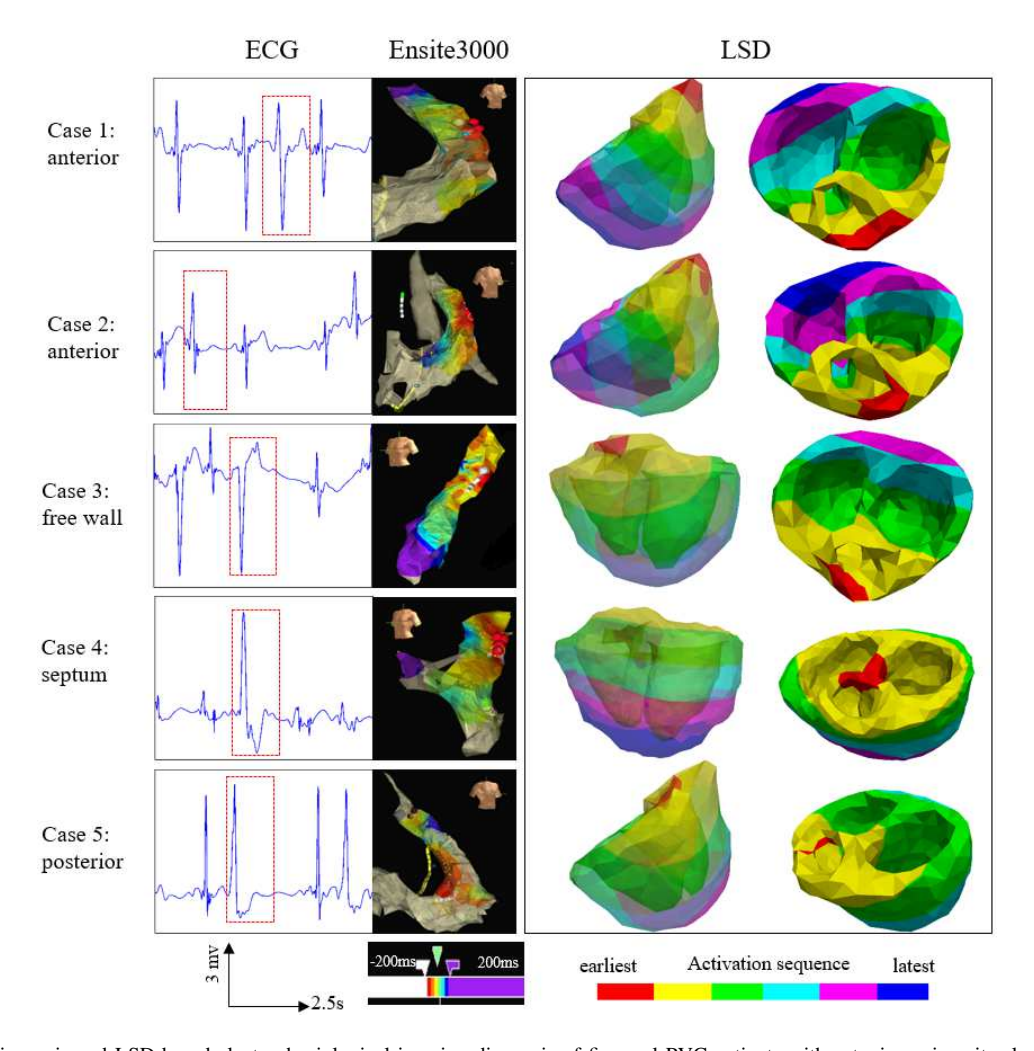


Fig. 10. Clinical diagnosis and LSD-based electrophysiological imaging diagnosis of five real PVC patients with ectopic pacing sites located at RVOT. The leftmost column indicates the ECGs measured by the 25th electrode on the body surface. The second column displays the RVOT models and activation maps reconstructed by the Ensite3000 system. The last two columns show the activation maps reconstructed by the proposed LSD method. Among them, the third column shows the ventricular geometric models from the orientation close to that of Ensite images, with an opacity of 0.47 in order to fluoroscopy the endocardium, and the last column is a top view.

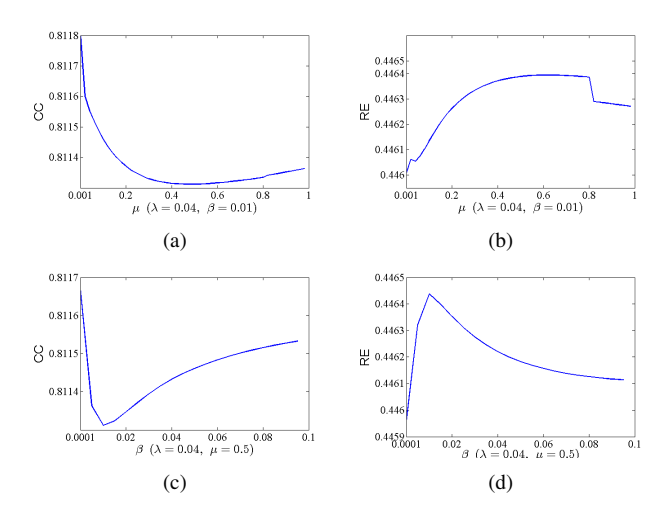


Fig. 11. CC and RE for different μ and β settings. (a), (b): μ is set within [0.001, 1] when β is fixed at 0.01. (c), (d): β is tested from 0.0001 to 0.1 when μ is fixed at 0.5.

To validate the accuracy of the LSD model for reconstructing cardiac surface potentials and localizing pacing sites, experiments were performed using simulated ventricular pacing, clinical interventional pacing, and clinical PVC data. In this paper, the test data belongs to clinical situation of single-site pacing or single-focus PVC. Future efforts will explore the performance of the LSD model in some complex heart rhythms such as multi-site pacing or structural disease.

V. CONCLUSION

In this paper, the LSD method has been proposed to overcome the ill-posed ECG inverse problem. Dynamic constraints and batch optimization are provided to obtain accurate endoepi potential reconstruction and precise localization of ectopic pacing sites. The proposed method combines multi-frame vectorized EEPs into a spatiotemporal image, and exploits the low-rank property of the background and detail sparseness of the spatiotemporal distribution. The simulation experiments on EEP reconstruction with different pacing sites demonstrate that the proposed method can improve the EEP reconstruction accuracy compared to conventional methods based on the L2norm and L1-norm. Experiments on real PVC subjects confirm that the LSD algorithm can correctly expose the locations of ectopic pacing sites.

REFERENCES

- [1] E. Fetisova *et al.*, "Noninvasive ecg imaging visualises rotors and multiple wavelets in patients with ventricular fibrillation," *Journal of Atrial Fibrillation*, vol. 8, no. S1, pp. 1–1, 2015.
- [2] S. Ghosh and Y. Rudy, "Application of 11-norm regularization to epicardial potential solution of the inverse electrocardiography problem," *Annals of biomedical engineering*, vol. 37, no. 5, pp. 902–912, 2009.
- [3] L. Wang et al., "Noninvasive epicardial and endocardial electrocardiographic imaging of scar-related ventricular tachycardia," *Journal of electrocardiology*, vol. 49, no. 6, pp. 887–893, 2016.
- [4] W. Einthoven, "Die galvanometrische registrirung des menschlichen elektrokardiogramms, zugleich eine beurtheilung der anwendung des capillar-elektrometers in der physiologie," Archiv für die gesamte Physiologie des Menschen und der Tiere, vol. 99, no. 9-10, pp. 472–480, 1903.
- [5] A. A. Armoundas et al., "A single equivalent moving dipole model: an efficient approach for localizing sites of origin of ventricular electrical activation," Annals of Biomedical Engineering, vol. 31, no. 5, pp. 564– 576, 2003.
- [6] R. M. Gulrajani et al., "Moving dipole inverse ecg and eeg solutions," IEEE Transactions on Biomedical Engineering, no. 12, pp. 903–910, 1084
- [7] J. Svehlikova et al., "Noninvasive identification of two lesions with local repolarization changes using two dipoles in inverse solution simulation study," Computers in biology and medicine, vol. 57, pp. 96–102, 2015.
- [8] —, "Classification of inverse solutions to two dipoles," in Computing in Cardiology Conference (CinC), 2013. IEEE, 2013, pp. 1127–1130.
- [9] Y. Rudy, "Noninvasive electrocardiographic imaging of arrhythmogenic substrates in humans," *Circulation research*, vol. 112, no. 5, pp. 863– 874, 2013.
- [10] A. N. Tikhonov and V. Y. Arsenin, "Solution of ill-posed problems," Mathematics of Computation, vol. 32, no. 144, pp. 491–491, 1977.
- [11] P. C. Franzone, "Some inverse problems in electrocardiology," in Numerical Treatment of Inverse Problems in Differential and Integral Equations. Springer, 1983, pp. 180–205.
- [12] Y. Saad and M. H. Schultz, "Gmres: A generalized minimal residual algorithm for solving nonsymmetric linear systems," SIAM Journal on scientific and statistical computing, vol. 7, no. 3, pp. 856–869, 1986.
- [13] C. Ramanathan et al., "Noninvasive electrocardiographic imaging (ecgi): application of the generalized minimal residual (gmres) method," Annals of biomedical engineering, vol. 31, no. 8, pp. 981–994, 2003.
- [14] L. Wang et al., "Application of 11-norm regularization to epicardial potential reconstruction based on gradient projection," *Physics in Medicine & Biology*, vol. 56, no. 19, p. 6291, 2011.
- [15] G. Shou et al., "Total variation regularization in electrocardiographic mapping," in *Life System Modeling and Intelligent Computing*. Springer, 2010, pp. 51–59.
- [16] B. Erem et al., "Using transmural regularization and dynamic modeling for noninvasive cardiac potential imaging of endocardial pacing with imprecise thoracic geometry," *IEEE transactions on medical imaging*, vol. 33, no. 3, pp. 726–738, 2014.
- [17] L. Wang, "Personalized noninvasive imaging of volumetric cardiac electrophysiology," 2009.
- [18] F. Greensite, "Two mechanisms for electrocardiographic deconvolution," in Engineering in Medicine and Biology Society, 1996. Bridging Disciplines for Biomedicine. Proceedings of the 18th Annual International Conference of the IEEE, vol. 4. IEEE, 1996, pp. 1425–1426.
- [19] P. M. Van Dam et al., "Non-invasive imaging of cardiac activation and recovery," Annals of biomedical engineering, vol. 37, no. 9, pp. 1739– 1756, 2009.
- [20] P. M. van Dam et al., "Quantitative localization of premature ventricular contractions using myocardial activation ecgi from the standard 12-lead electrocardiogram," *Journal of electrocardiology*, vol. 46, no. 6, pp. 574– 579, 2013.
- [21] B. Erem et al., "Identifying model inaccuracies and solution uncertainties in non-invasive activation-based imaging of cardiac excitation using convex relaxation," *IEEE transactions on medical imaging*, vol. 33, no. 4, p. 902, 2014.

- [22] B. Tilg et al., "Model-based imaging of cardiac electrical excitation in humans," *IEEE transactions on medical imaging*, vol. 21, no. 9, pp. 1031–1039, 2002.
- [23] P. Oosterhoff et al., "Experimental validation of noninvasive epicardial and endocardial activation imaging," Circulation: Arrhythmia and Electrophysiology, vol. 9, no. 8, p. e004104, 2016.
- [24] D. Potyagaylo et al., "Influence of modeling errors on the initial estimate for nonlinear myocardial activation times imaging calculated with fastest route algorithm," *IEEE Transactions on Biomedical Engineering*, vol. 63, no. 12, pp. 2576–2584, 2016.
- [25] L. Yu et al., "Three-dimensional noninvasive imaging of ventricular arrhythmias in patients with premature ventricular contractions," *IEEE Transactions on Biomedical Engineering*, 2017.
- [26] G. Li and B. He, "Localization of the site of origin of cardiac activation by means of a heart-model-based electrocardiographic imaging approach," *IEEE transactions on biomedical engineering*, vol. 48, no. 6, pp. 660–669, 2001.
- [27] C. Han et al., "Noninvasive reconstruction of the three-dimensional ventricular activation sequence during pacing and ventricular tachycardia in the canine heart," American Journal of Physiology-Heart and Circulatory Physiology, vol. 302, no. 1, pp. H244–H252, 2011.
- [28] L. Yu et al., "Temporal sparse promoting three dimensional imaging of cardiac activation," *IEEE transactions on medical imaging*, vol. 34, no. 11, pp. 2309–2319, 2015.
- [29] T. Yang et al., "Noninvasive activation imaging of ventricular arrhythmias by spatial gradient sparse in frequency domain-application to mapping reentrant ventricular tachycardia," *IEEE transactions on medical imaging*, 2018.
- [30] Z. Liu et al., "Noninvasive reconstruction of three-dimensional ventricular activation sequence from the inverse solution of distributed equivalent current density," *IEEE transactions on medical imaging*, vol. 25, no. 10, pp. 1307–1318, 2006.
- [31] C. Liu and B. He, "Noninvasive estimation of global activation sequence using the extended kalman filter," *IEEE Transactions on Biomedical Engineering*, vol. 58, no. 3, pp. 541–549, 2011.
- [32] P. Lander and E. Berbari, "Contouring of epicardial activation using spatial autocorrelation estimates," in *Computers in Cardiology 1991*, *Proceedings*. IEEE, 1991, pp. 541–544.
- [33] R. S. MacLeod and D. H. Brooks, "Recent progress in inverse problems in electrocardiology," *IEEE Engineering in Medicine and Biology Magazine*, vol. 17, no. 1, pp. 73–83, 1998.
- [34] M. Potse et al., "Cardiac anisotropy in boundary-element models for the electrocardiogram," Medical & biological engineering & computing, vol. 47, no. 7, pp. 719–729, 2009.
- [35] J. Yang and X. Yuan, "Linearized augmented lagrangian and alternating direction methods for nuclear norm minimization," *Mathematics of computation*, vol. 82, no. 281, pp. 301–329, 2013.
- [36] E. J. Candès et al., "Robust principal component analysis?" Journal of the ACM (JACM), vol. 58, no. 3, p. 11, 2011.
- [37] S. Boyd et al., "Distributed optimization and statistical learning via the alternating direction method of multipliers," Foundations and Trends® in Machine learning, vol. 3, no. 1, pp. 1–122, 2011.
- [38] J.-F. Cai et al., "A singular value thresholding algorithm for matrix completion," SIAM Journal on Optimization, vol. 20, no. 4, pp. 1956– 1982, 2010.
- [39] P. C. Hansen and D. P. OLeary, "The use of the 1-curve in the regularization of discrete ill-posed problems," SIAM Journal on Scientific Computing, vol. 14, no. 6, pp. 1487–1503, 1993.
- [40] K. Aras et al., "Experimental data and geometric analysis repositoryedgar," *Journal of electrocardiology*, vol. 48, no. 6, pp. 975–981, 2015.
- [41] A. Loewe et al., "Ecg-based detection of early myocardial ischemia in a computational model: impact of additional electrodes, optimal placement, and a new feature for st deviation," BioMed research international, vol. 2015, 2015.
- [42] W. H. Schulze et al., "A simulation dataset for ecg imaging of paced beats with models for transmural, endo-and epicardial and pericardial source imaging," Germany: Bad Herrenalb, 2015.
- [43] B. Akdemir et al., "Premature ventricular contractions: Reassure or refer?" Cleveland Clinic journal of medicine, vol. 83, no. 7, p. 525, 2016.
- [44] P. S. Cuculich *et al.*, "Noninvasive characterization of epicardial activation in humans with diverse atrial fibrillation patterns," *Circulation*, vol. 122, no. 14, pp. 1364–1372, 2010.